Cell Reports

Article

Intertwined Wdr47-NTD dimer recognizes a basic-helical motif in Camsap proteins for proper central-pair microtubule formation

Graphical abstract

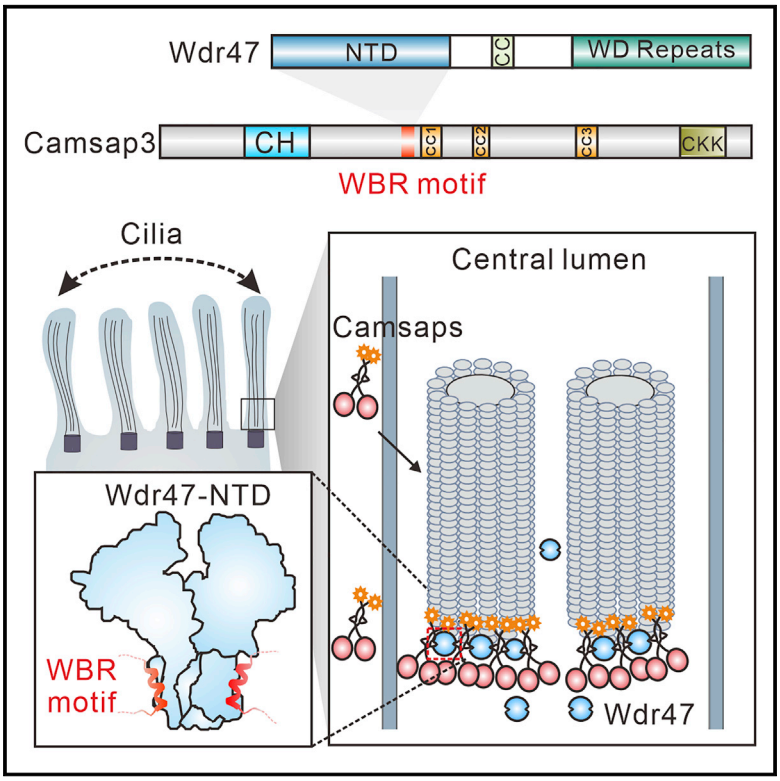

Highlights

- Wdr47-NTD forms an intertwined dimer with a special sub-domain organization
- Wdr47-NTD recognizes a basic helical motif (the WBR peptide) in Camsap proteins
- The WBR peptide anchors into a non-canonical target-binding pocket in Wdr47-NTD
- Wdr47-NTD-mediated association of Camsaps is essential for proper CP-MT formation

Authors

Jinqi Ren, Dong Li, Juyuan Liu, Hao Liu, Xiumin Yan, Xueliang Zhu, Wei Feng

Correspondence

xlzhu@sibcb.ac.cn (X.Z.),
wfeng@ibp.ac.cn (W.F.)

In brief

Camsap proteins bind to Wdr47-NTD to properly generate axonemal CP-MTs. Ren et al. present the structures of apo-Wdr47-NTD and Wdr47-NTD in complex with the WBR peptide from Camsap3 and observe that the intertwined Wdr47-NTD dimer recognizes the characteristic WBR peptide via a non-canonical target-binding site for proper CP-MT formation.

Ren et al., 2022, Cell Reports *41*, 111589
November 8, 2022
https://doi.org/10.1016/j.celrep.2022.111589

CellPress

Cell Reports

CellPress
OPEN ACCESS

Article

Intertwined Wdr47-NTD dimer recognizes a basic-helical motif in Camsap proteins for proper central-pair microtubule formation

Jinqi Ren,[1,4] Dong Li,[1,3,4] Juyuan Liu,[2,3,4] Hao Liu,[2] Xiumin Yan,[2] Xueliang Zhu,[2,3,*] and Wei Feng[1,3,5,*]

[1]National Laboratory of Biomacromolecules, CAS Center for Excellence in Biomacromolecules, Institute of Biophysics, Chinese Academy of Sciences, 15 Datun Road, Beijing 100101, China

[2]State Key Laboratory of Cell Biology, Shanghai Institute of Biochemistry and Cell Biology, Center for Excellence in Molecular Cell Science, Chinese Academy of Sciences, 320 Yueyang Road, Shanghai 200031, China

[3]College of Life Sciences, University of Chinese Academy of Sciences, Beijing 100049, China

[4]These authors contributed equally

[5]Lead contact

*Correspondence: xlzhu@sibcb.ac.cn (X.Z.), wfeng@ibp.ac.cn (W.F.)

https://doi.org/10.1016/j.celrep.2022.111589

SUMMARY

Calmodulin-regulated spectrin-associated proteins (Camsaps) bind to the N-terminal domain of WD40-repeat 47 (Wdr47-NTD; featured with a LisH-CTLH motif) to properly generate axonemal central-pair microtubules (CP-MTs) for the planar beat pattern of mammalian motile multicilia. The underlying molecular mechanism, however, remains unclear. Here, we determine the structures of apo-Wdr47-NTD and Wdr47-NTD in complex with a characteristic Wdr47-binding region (WBR) from Camsap3. Wdr47-NTD forms an intertwined dimer with a special cross-over region (COR) in addition to the canonical LisH and globular α-helical core (GAC). The basic WBR peptide adopts an α-helical conformation and anchors to a tailored acidic pocket embedded in the COR. Mutations in this target-binding pocket disrupt the interaction between Wdr47-NTD and Camsap3. Impairing Wdr47-Camsap interactions markedly reduces rescue effects of Wdr47 on CP-MTs and ciliary beat of *Wdr47*-deficient ependymal cells. Thus, Wdr47-NTD functions by recognizing a specific basic helical motif in Camsap proteins via its non-canonical COR, a target-binding site in LisH-CTLH-containing domains.

INTRODUCTION

The axoneme of motile cilia and flagella is an exquisite microtubule (MT)-based structure that exhibits oscillatory beating to drive cell movement or extracellular fluid flow (Brooks and Wallingford, 2014; Ginger et al., 2008; Ishikawa, 2017; Satir and Christensen, 2007). It mostly consists of nine peripheral doublet MTs (with the attachment of two rows of dynein arms) and a central pair (CP) of singlet MTs (Ishikawa, 2017; Satir et al., 2014). CP-MTs are associated with specific projections and bridges to form an inner CP apparatus that communicates with the radial spokes (RSs) protruding from outer doublet MTs (Loreng and Smith, 2017; Satir et al., 2014). The CP-RS connection system is proposed to work as a distributor to sense chemical and mechanical signals and regulate dynein-arm activities for ciliary motility (Lindemann, 2007; Oda et al., 2014; Zhu et al., 2017). Given their prominent roles in ciliary beating, the lack or even partial defect of CP-MTs in the axoneme alters the ciliary beat pattern, resulting in primary ciliary dyskinesia (PCD) in humans with characteristics of recurrent respiratory infections, infertility, or hydrocephalus (Fliegauf et al., 2007; Praveen et al., 2015; Stannard et al., 2004).

CP-MTs are non-centrosomal MTs, with their minus ends sitting above the transition zone and their plus ends extending to the ciliary tip (Loreng and Smith, 2017). Since the minus ends are not attached to the basal body, CP-MTs in protozoa are thought to originate from preassembled MT seeds or self-assemble *de novo* from a high concentration of tubulins in the axonemal lumen (Lechtreck et al., 2013; Loreng and Smith, 2017). These MT seeds and tubulins are suggested to be generated by intraflagellar transport-mediated import or katanin-mediated severing of axonemal MTs (Dymek et al., 2004; Dymek and Smith, 2012). Calmodulin-regulated spectrin-associated proteins (Camsaps)/patronin family proteins (Camsap1–3 in mammals) are metazoan katanin-binding partners that specifically recognize and stabilize MT minus ends for assembling non-centrosomal MTs (Akhmanova and Steinmetz, 2015; Hendershott and Vale, 2014; Jiang et al., 2014). The MT-minus-end recognition capacity of Camsaps is contributed by the C-terminal family-specific Camsap1, KIAA1078, KIAA1543 (CKK) domain (Akhmanova and Hoogenraad, 2015; Atherton et al., 2017; Baines et al., 2009). Given their essential roles in assembling non-centrosomal MTs, Camsaps are involved in organizations of MT arrays in polarized cells such as neurons and

epithelia (Pongrakhananon et al., 2018; Toya et al., 2016; Yau et al., 2014). More intriguingly, Camsap3 is critical for the formation of CP-MTs and proper orientation of the basal body in motile cilia (Robinson et al., 2020).

WD40-repeat 47 (Wdr47; also called Nemitin) is a WD40-repeat-containing protein that associates with MTs through MT-associated protein 8 (MAP8) (Wang et al., 2012). Wdr47 functions in the neural stem cell proliferation and growth-cone dynamics by enhancing MT stability, possibly through its inhibition of superior cervical ganglion-10 (SCG10), a well-known MT-destabilizing protein (Kannan et al., 2017). Wdr47 is also critical for neuronal polarization by interacting with Camsaps to fine-tune MT dynamics of neurites (Buijs et al., 2021; Chen et al., 2020). Intriguingly, Wdr47 is essential for CP-MT formation through the Camsap-katanin axis: katanin generates MT seeds by probably severing peripheral axonemal MTs, Camsaps stabilize these seeds to allow their elongations, and Wdr47 enriches Camsaps into the axonemal central lumen to ensure highly efficient and accurate CP-MT formation (Liu et al., 2021). Conventional or neural tissue-specific *Wdr47*-deficient mice die of suffocation quickly after birth (Chen et al., 2020), whereas compound mutant mice or glia/ependyma-specific *Wdr47*-deficient mice manifest severe hydrocephaly and short lifespan (Chen et al., 2020; Liu et al., 2021). Multicilia in *Wdr47*-deficient multiciliated cells completely lack CP-MTs and display an abnormal rotational, rather than the normal back-and-forth (planar), beat pattern (Liu et al., 2021). Elevating the total levels of Camsaps rescues the CP-MT formation at the expense of low efficiency and a high incidence of wrong numbers and locations (Liu et al., 2021).

Wdr47 contains an N-terminal domain (NTD) featured with a lissencephaly type-1-like homology (LisH)-C-terminal to LisH (CTLH) motif. Wdr47-NTD specifically recognizes a short region in Camsaps (Liu et al., 2021), denoted herein as the Wdr47-binding region (WBR). The molecular mechanism underlying the Wdr47-Camsap interaction, however, remain largely unclear. In this study, we determine the structures of apo-Wdr47-NTD (i.e., Wdr47-NTD without the binding of the WBR peptide) and Wdr47-NTD in complex with the WBR peptide from Camsap3. Wdr47-NTD forms an intertwined dimer with a special organization of three sub-domains: LisH, globular α-helical core (GAC), and cross-over region (COR). Unexpectedly, the basic WBR peptide adopts an α-helical conformation and anchors to a tailored acidic pocket in COR (rather than the canonical target-binding sites in GAC). Mutations in this COR pocket disrupt the interactions between Wdr47 and Camsaps and impair the Wdr47-mediated regulation of CP-MTs and ciliary motility. Thus, Wdr47-NTD recognizes a basic helical motif in Camsaps via the non-canonical pocket in COR for the Wdr47-Camsap complex assembly.

RESULTS AND DISCUSSION

Structure of Wdr47-NTD containing the LisH-CTLH motif

Since Wdr47-NTD contains the signature LisH-CTLH motif, which is not well characterized (Figure 1A), we initiated this work to characterize it biochemically and structurally. Based on the primary sequence analysis, the fragment of Wdr47-NTD contains residues 1–315 including the LisH-CTLH motif and the C-terminal extended region with predicted secondary structures (Figures 1A and S1). Consistent with the capacity of the LisH-CTLH motif for self-association (Emes and Ponting, 2001), Wdr47-NTD primarily exists as a dimer in solution (Figure 1B). The high quality of the Wdr47-NTD protein sample encouraged us to perform crystal screening of this fragment, and the crystals of Wdr47-NTD were obtained for structural determination. The structure of Wdr47-NTD was determined by the single-wavelength anomalous dispersion (SAD) method and was refined to 3.1 Å (Figure 1C; Table 1). Consistent with the dimeric state in solution, one dimer with two Wdr47-NTD molecules was found in the asymmetric unit of the crystal. In this dimer structure, the extreme N terminus, a stretch of the C-terminal tail, and several internal loops of Wdr47-NTD could not be resolved due to their poor electron density maps, and the structure comprises residues from 6 to 292 while missing several flexible loops (as indicated by dashed lines in Figure 1C).

In the dimer structure, Wdr47-NTD is composed of twelve α-helices (α1 to α12) and two β-strands (β1 and β2) and can be divided into three sub-domains: LisH, GAC, and COR (Figures 1C, 1D, and S1). LisH contains two α-helices (α1 and α2) and two LisHs arranged in an anti-parallel manner to form a four-helix bundle in the center of the dimer; GAC is composed of six α-helices (α3 to α8, with the first three α-helices from CTLH) and forms a globular structure sitting above each LisH; and COR is constructed by three α-helices (α9 to α11), and two CORs cross over each other to form an intertwined dimer that intimately holds two LisHs (the central four-helix bundle) with each of two lateral sites covered by two parallel β-strands (β1 and β2) (Figures 1C–1E). Moreover, the extreme C-terminal helix (α12) of Wdr47-NTD folds back to pack with GAC, and two terminal helices anti-parallelly insert into the central cavity formed between two GACs in the dimer (Figure 1F). Thus, the three sub-domains of Wdr47-NTD are arranged in an integrated manner to form an intertwined dimer with the aid of LisH and COR.

Special sub-domain organization in the Wdr47-NTD dimer

Wdr47-NTD is a LisH-CTLH-containing domain and forms an intertwined dimer with a compact conformation (Figure 1F). To generalize the feature of the LisH-CTLH motif, we compared the structure of the Wdr47-NTD dimer with that of the LisH-CTLH-containing domains from Smu1 and TPL (Martin-Arevalillo et al., 2017; Ulrich et al., 2016) (Figure S2A). Similar to Wdr47, Smu1 and TPL both contain a LisH-CTLH motif in their NTDs that adopt a dimeric conformation (Figure S2B). In the structures of Smu1-NTD and TPL-NTD, LisH forms a similar central four-helix bundle in the center of the dimer, supporting the intrinsic capacity of LisH for self-association; and CTLH is composed of three α-helices that integrate with following α-helices to assemble a globular fold GAC, indicating that GAC is a general sub-domain for LisH-CTLH-containing domains (Figure S2B). However, the orientation between LisH and GAC in these structures seems not to be fixed, i.e., GAC does not contact with LisH in Smu1-NTD but packs with LisH in TPL-NTD and Wdr47-NTD, and two GACs in these dimers are likely to undergo a rotation from an open-wide to a closed-compact conformation

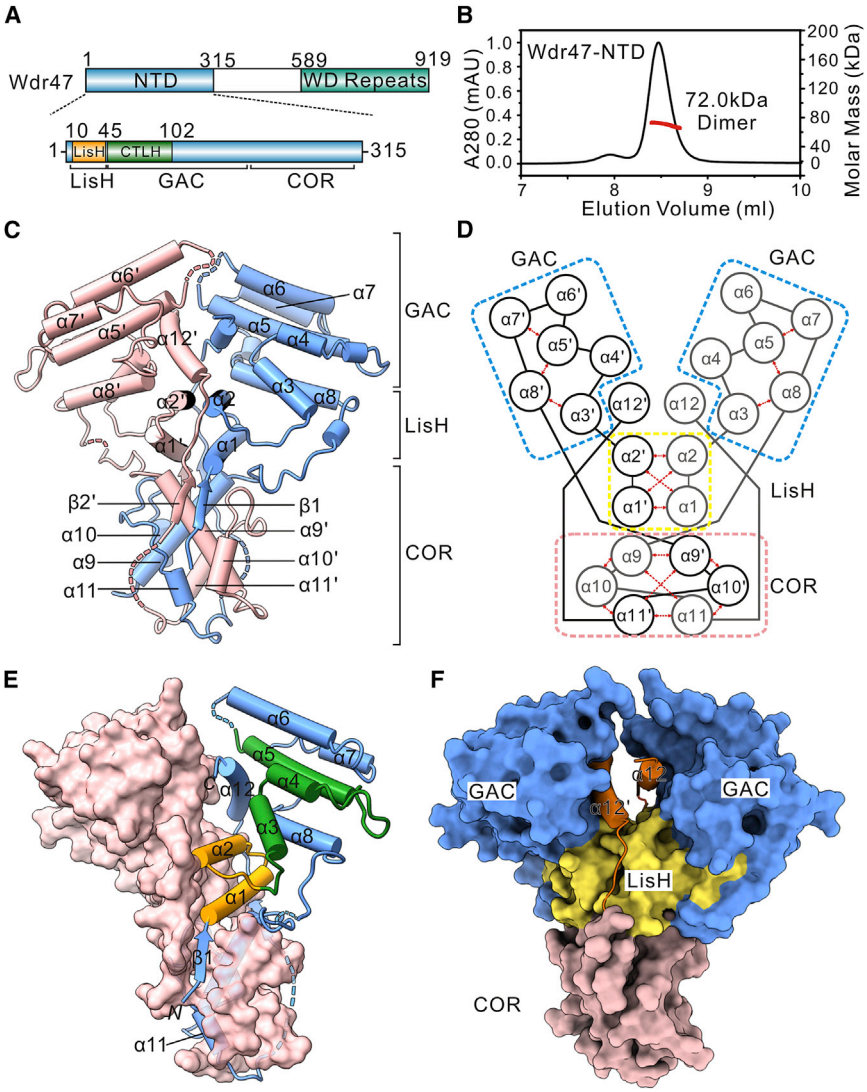

Figure 1. Structure of the intertwined Wdr47-NTD dimer

(A) Domain organization of Wdr47. Wdr47 contains an N-terminal domain (NTD) featured with a LisH-CTLH motif and a WD40-repeat domain at the C terminus. The construct of Wdr47-NTD used for crystallization is indicated.

(B) Biochemical characterization of the oligomeric state of Wdr47-NTD by size-exclusion chromatography-multi-angle light scattering (SEC-MALS). The calculated molecular weight of Wdr47-NTD matches a dimeric state.

(C) Overall structure of the Wdr47-NTD dimer. A ribbon diagram of the Wdr47-NTD dimer structure with the two protomers colored in pink and light blue, respectively.

(D) A schematic representation of the sub-domain organization of the Wdr47-NTD dimer. Wdr47-NTD contains three sub-domains (LisH, GAC, and COR). LisH contains two α-helices (α1 and α2), GAC is composed of six α-helices (α3 to α8), and COR is constructed by three α-helices (α9 to α11).

(E and F) A combined surface and ribbon diagram of the Wdr47-NTD dimer structure. The two protomers of the Wdr47-NTD dimer are intertwined by the LisH and COR sub-domains, and the extreme C-terminal helix folds back to insert into a central cavity formed between the two GAC sub-domains in the dimer.

See also Figures S1–S3.

(Figures 1F and S2B). On the other hand, the most striking difference in these dimeric structures is the conformation of COR. In Smu1-NTD and TPL-NTD, COR is only composed of a single α-helix that crosses over to loosely pack with LisH in the dimer, but in Wdr47-NTD, COR is much complicated and is constructed by three α-helices and one β-strand that intertwine to tightly integrate with LisH for dimer formation (Figures 1F and S2B). Thus, compared with Smu1-NTD and TPL-NTD, Wdr47-NTD contains a special sub-domain organization with an expanded version of COR for intertwined dimerization.

Integration of LisH and COR for intertwined dimerization of Wdr47-NTD

In the Wdr47-NTD dimer, two protomers are similar and can be well superimposed with each other (with a root-mean-square deviation [RMSD] of ~1.86 Å for backbone atoms) (Figure S3A). In each protomer, GAC forms a well-folded globular structure, but LisH and COR adopt a partially folded conformation for assembling the intertwined dimer (Figure S3A). The formation of the Wdr47-NTD dimer is contributed by the packing of partially folded LisH and COR in the protomer into a well-folded structure in the dimer (Figure S3A). Consistently, the dimer interfaces are composed of the residues from LisH that construct the hydrophobic packing core of the central four-helix bundle and of the residues from COR that organize an extensive hydrophobic packing network between the intertwined dimer (Figures S3B–S3D). In addition to these intra-sub-domain packings, the intersub-domain contacts between LisH and COR are comprised by the hydrophobic residues from each sub-domain and are likely to be zipped by a pair of β-strands formed between the N-terminal extension of LisH and the C-terminal tail of COR (Figures S3E and 1C). Thus, the dimerization of Wdr47-NTD resembles a structural folding process mediated by LisH and COR, and the integration of these two sub-domains contributes to the formation of the intertwined dimer.

On the other hand, GAC seems to have few contributions to the dimerization of Wdr47-NTD but also packs with LisH and the C-terminal helix in the dimer (Figures S3F–S3G). The inter-sub-domain contacts between GAC and LisH are mediated by the hydrophobic and hydrogen-bonding interactions, and these contacts support the closed-compact conformation of two

Table 1. Data collection and structural refinement statistics

	Apo-Wdr47-NTD	Wdr47-NTD/Camsap3 WBR peptide
Data collection		
Space group	$P2_12_12_1$	$P2_12_12_1$
Cell dimensions		
a, *b*, *c* (Å)	57.4, 75.8, 170.0	58.1, 105.3, 156.0
α, β, γ (°)	90, 90, 90	90, 90, 90
Resolution (Å)	50.0–3.1 (3.21–3.10)[a]	30.0–3.2 (3.31–3.20)
R_{merge}	0.087 (0.872)	0.071 (0.817)
$I/\sigma(I)$	13.1 (1.4)	18.3 (1.1)
Completeness (%)	98.4 (97.8)	99.8 (99.9)
Redundancy	6.9 (6.0)	6.7 (7.0)
Refinement		
Resolution (Å)	37.1–3.1 (3.2–3.1)	24.2–3.2 (3.3–3.2)
No. reflections	13,899 (1,352)	16,101 (1,504)
R_{work}/R_{free}(%)	25.6/29.0	27.1/31.4
No. atoms		
Protein	4,179	4,227
Water	0	0
B-factors		
Protein	99.3	99.4
RMSDs		
Bond lengths (Å)	0.002	0.003
Bond angles (°)	0.42	0.53

[a]Values in parentheses are for highest-resolution shell.

GACs in the Wdr47-NTD dimer (compared with the Smu1-NTD and TPL-NTD dimers) (Figures S2B and S3F). However, the contacts between GAC and the C-terminal helix are much looser, with a few pairs of hydrogen bonds, indicating that the packing between them is not tight but dynamic (Figure S3G, and see below for details).

Wdr47-NTD-binding region in Camsap3

Our previous study suggests that Camsaps display redundant functions in the CP-MT formation (Liu et al., 2021). Currently only *Camsap3* deficiency alone has been documented to impair the CP-MT formation, mainly in murine nasal multiciliated cells (Kimura et al., 2021; Robinson et al., 2020; Usami et al., 2021). We thus decided to focus on the Camsap3-Wdr47 interaction. Consistent with our previous results that a fragment in the central unstructured region of Camsap1 (residues 312–858) can bind to Wdr47-NTD (Liu et al., 2021), the glutathione S-transferase (GST) pull-down assay, using a series of Camsap3 truncations, indicated that a homologous fragment in the middle region (residues 351–593) binds to Wdr47-NTD (Figures S4A–S4C). To determine the minimum region in Camsap3 for binding to Wdr47-NTD, a number of truncations were further designed in this fragment based on the primary sequence analysis and checked by the GST pull-down assay. The minimum Wdr47-NTD-binding region in Camsap3 was narrowed down to a short fragment (residues 561–590) close to the central predicted coiled-coil segment, referred to as the WBR peptide (Figure S4C). We then commercially synthesized this WBR peptide and measured the binding affinity for Wdr47-NTD by an isothermal titration calorimetry (ITC) assay. Consistent with the GST pull-down assay, the WBR peptide bound to WDR47-NTD with a high affinity (with a K_D of 5.9 ± 0.5 μM) (Figure S4D). Moreover, the primary sequence of the WBR-peptide was found to be highly conserved among three Camsaps (Figure S4B), suggesting that the Wdr47-NTD-binding region derived from Camsap3 could be applicable to other Camsaps.

Structure of Wdr47-NTD in complex with the WBR peptide from Camsap3

To investigate the mechanism underlying the WBR-peptide recognition by Wdr47-NTD, we further performed crystal screening of Wdr47-NTD in complex with the WBR peptide from Camsap3 (Figure 2A). With co-crystallization of Wdr47-NTD and the synthetic WBR peptide, the crystals of the Wdr47-NTD/WBR peptide complex were obtained for structural determination. The structure of the complex was determined by the molecular replacement method and was refined to 3.2 Å (Figure 2B; Table 1). The WBR peptide of Camsap3 was resolved (from 565 to 580) based on its electron density map (Figure 2C). Consistent with the dimeric conformation of Wdr47-NTD, two WBR peptides symmetrically bind to the Wdr47-NTD dimer (Figure 2B). However, one of these two WBR peptides could not be well traced due to the poor quality of the electron density map, and therefore, the well-resolved WBR peptide with the high quality of the electron density map was chosen for further structural analysis (Figure S5A).

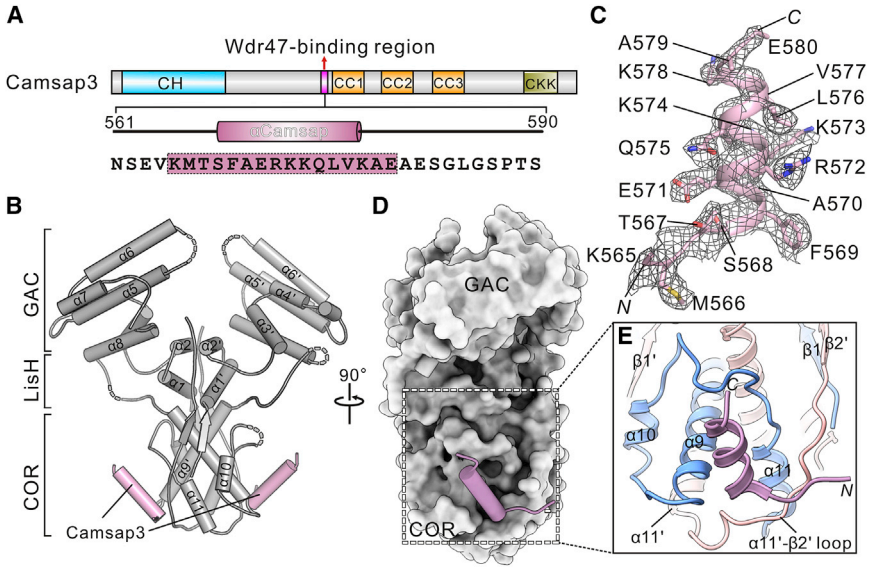

Figure 2. Structure of the Wdr47-NTD/WBR peptide complex

(A) Domain organization of Camsap3. Camsap3 contains an N-terminal CH domain, three conserved coiled coils (CC1–CC3), and a C-terminal CKK domain. The Wdr47-binding region (WBR) is located in the middle, and the WBR peptide from Camsap3 used for crystallization is indicated.

(B) Overall structure of Wdr47-NTD in complex with the WBR peptide from Camsap3. A ribbon diagram of the Wdr47-NTD/WBR peptide complex structure. Wdr47-NTD and the WBR peptide are colored in gray and pink, respectively.

(C) The omit electron density map of the WBR peptide (from K565 to E580) contoured at 1.0 σ level.

(D and E) A combined surface and ribbon diagram of the complex structure. The WBR peptide inserts into a tailored pocket in the COR sub-domain of the Wdr47-NTD dimer (D), which is constructed by the three short helices α9–α11 (from one protomer) and the α11/β2-loop (from the other one) (E).

See also Figures S4–S6.

In the complex structure, the WBR peptide adopts an α-helical conformation and directly inserts into a tailored pocket in the COR sub-domain of Wdr47-NTD (Figure 2D). The WBR-peptide-binding pocket in the COR sub-domain is formed by the three short helices α9–α11 (from one protomer) and the α11/β2-loop (from the other one) that wrap around the helical WBR peptide (Figure 2E). On the other hand, Wdr47-NTD adopts a similar dimeric conformation organized by three sub-domains (LisH, GAC, and COR) but with a lack of the C-terminal helix (α12) existing in apo-Wdr47-NTD (Figure 2B). To further dissect the potential conformational changes of the Wdr47-NTD dimer induced by the binding of the WBR peptide, we superimposed the structure of the Wdr47-NTD/WBR peptide complex with that of apo-Wdr47-NTD by one protomer (Figure S5B). Interestingly, both LisH and COR exhibit few conformational changes upon the binding of the WBR peptide, but GAC undergoes an obvious local conformational change with a rotation of ~10° outward (Figure S5B). This local rotation would lead to the opening of the central cavity formed between two GACs in the dimer, in which two C-terminal helices are located (Figure S5B). Given the loose contacts between GAC and the C-terminal helix (Figure S3G), the local conformational change of GAC in the complex structure would likely unleash the folded-back C-terminal helix (Figure S5B), which may provide an explanation for the missing last helix. Nevertheless, the functional importance of these structural changes of Wdr47-NTD with the binding of the WBR peptide is currently unknown and awaits further investigations.

Non-canonical target-binding pocket in COR for the WBR peptide

In the structure of the Wdr47-NTD/WBR peptide complex, the binding pocket for the WBR peptide is unexpectedly located in the COR sub-domain (Figure 2E). However, this COR-mediated target-recognition mode is distinct from that in other LisH-CTLH-containing domains (Smu1-NTD and TPL-NTD) (Ashraf et al., 2019; Martin-Arevalillo et al., 2017) (Figure S6). Smu1-NTD contains two different sites for recognizing the target-peptide, i.e., one in GAC that captures a short α-helix from the peptide, and the other in the N-terminal part of LisH that pairs with a short β-hairpin from the peptide to form a complementary β-sheet, while TPL-NTD only contains one site in GAC that can recognize a linear short target peptide (Figure S6). Although the exact sites are somewhat diverse, the common feature between Smu1-NTD and TPL-NTD is that both contain at least one target-binding site in GAC, suggesting that GAC is the canonical target-recognition sub-domain. In contrast, the GAC sub-domain of Wdr47-NTD is not involved in the binding of the WBR peptide (Figure 2B). Moreover, the two-stranded β-sheet in Wdr47-NTD resembles the complementary β-sheet in the Smu1-NTD/target peptide complex, suggesting that this target-binding site in Smu1-NTD is also unavailable in Wdr47-NTD (Figures 2B and S6). Taken together, compared with other LisH-CTLH-containing domains, Wdr47-NTD contains a non-canonical target-binding pocket in the expanded version of COR for recognizing the WBR peptide.

Interaction interface between Wdr47-NTD and the WBR peptide

The target-binding pocket in COR is located in the intertwined-dimer interface constructed by two protomers (α9–α11 from one, and the α11/β2-loop from the other) (Figure 2E). The helical WBR peptide anchors into this target-binding pocket, and the interaction interface can be divided into the hydrophobic packing and electrostatic interaction sites (Figures 3A–3C). In the hydrophobic packing site, F569 from the WBR peptide makes hydrophobic contacts with V208 and C211 from α9, L244 and W247 from α11, and F260 from the α11/β2-loop, and the bulky aromatic side chain of F569 resembles a key to insert into this hydrophobic pocket, which is further stabilized by the hydrogen bonds formed between the side chains of T567 and Q262 and between the backbones of T567 and F260 from the WBR peptide and the α11/β2-loop, respectively (Figure 3B). In the electrostatic interaction site, R572, K573, and K574 from the WBR peptide

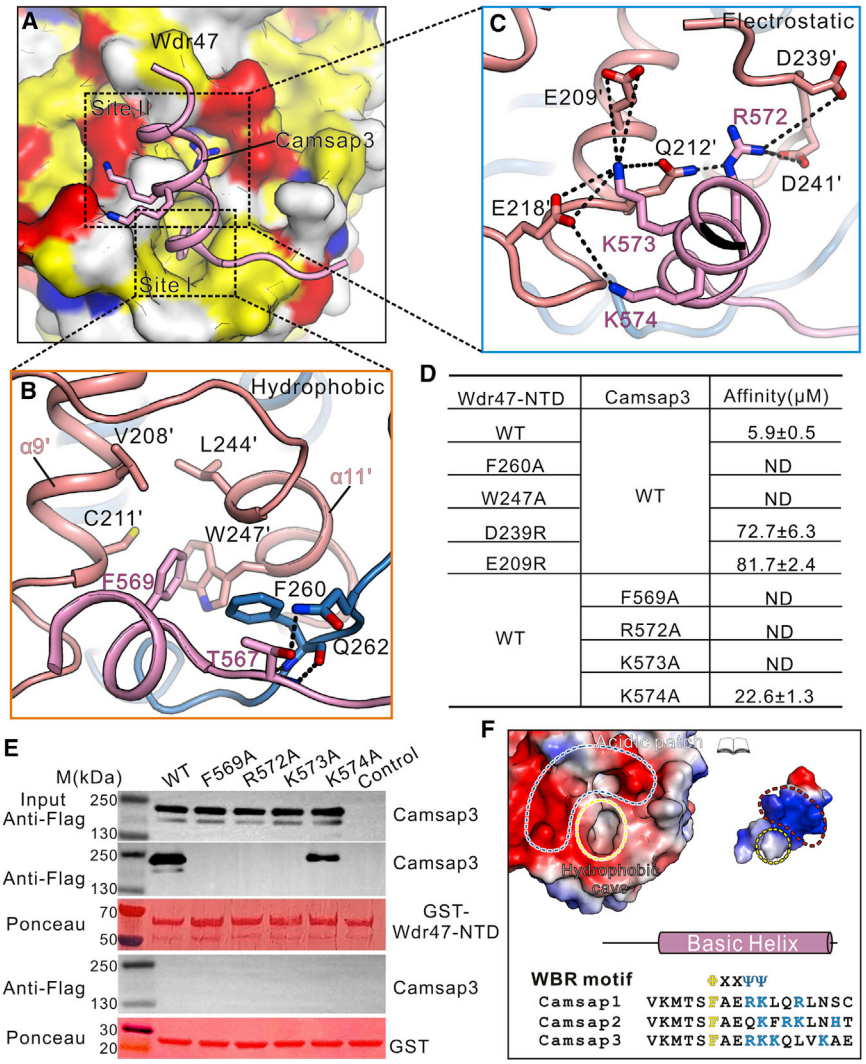

Figure 3. Interaction interface between Wdr47-NTD and the WBR peptide

(A) A combined surface and stick representation showing the interaction interface between Wdr47-NTD and the WBR peptide. The WBR peptide is in the stick representation (colored in pink), and Wdr47-NTD is in the surface representation (the hydrophobic, positively charged, and negatively charged residues and the rest of the residues are colored in yellow, blue, red, and white, respectively).

(B and C) A combined ribbon-and-stick model illustrates the interaction interface between Wdr47-NTD and the WBR peptide. Wdr47-NTD and the WBR peptide are colored in salmon and pink, respectively. The side chains of the residues involved in the interface packing are shown as sticks. Electrostatic and hydrogen-bonding interactions are indicated by dashed lines.

(D) A summary of the binding affinities between Wdr47-NTD (or its mutants) and the WBR peptide and that between Wdr47-NTD and the WBR peptide, with point mutations determined by the ITC assay. ND, not detectable.

(E) GST pull-down analysis of the interactions between Wdr47-NTD and full-length Camsap3 (and its mutants).

(F) The basic helical motif in Camsaps for Wdr47-NTD. In the surface representation, the positively and negatively charge potentials are colored in blue and red, respectively. In the sequence alignment, the conserved aromatic residue and positively charged residues are colored in yellow and blue, respectively.

See also Figure S7.

construct an electrostatic interaction network with E209 from α9, E218 from the α9/α10-loop, and D239 and D241 from the α10/α11-loop, and the side chains of R572 and K573 from the WBR peptide form the additional hydrogen bonds with the side chain of Q212 from α9 Figure 3C). Taken together, the extensive hydrophobic, electrostatic, and hydrogen-bonding interactions between the target-binding pocket of Wdr47-NTD and the WBR peptide contribute to the stable complex formation.

To evaluate the essential residues in the interaction interface for the complex formation, we made a series of point mutations in the target-binding pocket of Wdr47-NTD (i.e., F260A and W247A in the hydrophobic site, and D239R and E209R in the electrostatic site) and checked the binding between these Wdr47-NTD mutants and the WBR peptide by ITC assay (Figures 3B and 3C). All the point mutations in Wdr47-NTD abolished or severely impaired the binding of the WBR peptide (Figures 3D and S7A), confirming the essential role of these residues in the target-binding pocket for recognizing the WBR peptide. On the other hand, we made a series of point mutations in the WBR peptide (i.e., F569A in the hydrophobic site, and R572A, K573A, and K574A in the electrostatic site) and checked the binding to Wdr47-NTD by ITC assay (Figures 3B and 3C). Consistently, the F569A, R572A, and K573A mutations in the WBR peptide abolished the binding to Wdr47-NTD (Figures 3D and S7B), supporting the prominent roles of these residues in the WBR peptide for binding to Wdr47-NTD. In contrast, the K574A mutation mildly decreased the binding of the WBR peptide to Wdr47-NTD (Figures 3D and S7B), also consistent with the position of this residue in the periphery of the electrostatic interaction interface. To further check the essential roles of the residues in the interaction interfaces for Camsap3 to bind to Wdr47-NTD, we made the same set of point mutations in full-length Camsap3 and assessed the binding between Wdr47-NTD and Camsap3 by the GST pull-down assay (Figure 3E). Since the full-length Camsap3 could be hardly achieved, we used purified GST-tagged Wdr47-NTD to pull down the cell lysates with the expression of different mutants of FLAG-tagged Camsap3. Consistent with the ITC assay with the WBR peptide, compared with the wild-type protein, the F569A, R572A, and K573A mutants showed no bindings to Wdr47-NTD, while the K574A mutant retained certain binding capacity for Wdr47-NTD (Figure 3E). Taken together, the

residues in the interaction interface between Wdr47-NTD and the WBR peptide are essential for the binding between Wdr47-NTD and Camsap3.

The basic helical motif in Camsaps for Wdr47-NTD

In the structure of the Wdr47-NTD/WBR peptide complex, the target-binding pocket of Wdr47-NTD contains a small hydrophobic core surrounded by large negatively charged patches (Figure 3F). In accordance with this target-binding pocket, the WBR peptide from Camsap3 adopts an α-helical conformation with a characteristic aromatic residue at the beginning of the helix (for anchoring into the small hydrophobic core) and a number of positively charged residues following the aromatic residue (for contacting with the negatively charged patches) (Figure 3F). Based on the mutational studies of the WBR peptide, the aromatic residue and positively charged residues in this helix are essential for binding to Wdr47-NTD (Figures 3D and 3E), and a basic helical WBR motif in Camsap3 can be defined for Wdr47-NTD with the signature sequence "Φ-X-X-Ψ-Ψ" (Φ is an aromatic residue, and Ψ is a positively charged residue) (Figure 3F). Based on the primary sequence analysis, Camsap1 and Camsap2 also contain this basic helical WBR motif (Figures 3F and S4B). Specifically, the aromatic residue and the second positively charged residue in Camsap3 are extremely conserved in Camsap1 and Camsap2, while the first positively charged residue is only conserved in Camsap1 (Figure 3F). Although the third positively charged residue in Camsap3 (at the periphery of the electrostatic interaction interface) is not conserved, Camsap1 and Camsap2 contain additional positively charged residues in the following region, which may compensate for the missing third positively charged residue (Figure 3F). We next characterized the interactions between Wdr47-NTD and the WBR peptides from Camsap1 and Camsap2 by ITC assay (Figure S7C). As expected, compared with the WBR peptide from Camsap3, the WBR peptides from Camsap1 and Camsap2 showed similar binding affinities for Wdr47-NTD (with K_Ds of 3.4 ± 0.5 and 2.7 ± 0.8 μM, respectively) (Figure S7C). More importantly, the F206A mutation in the target-binding pocket of Wdr47-NTD also abolished the binding of the WBR-peptides from Camsap1 and Camsap2 (Figure S7C), supporting that the WBR motif in three Camsaps binds to Wdr47-NTD in a similar manner. Consistent with this structural analysis and biochemical characterization, Wdr47-NTD was shown to be capable of recognizing all the three Camsaps for controlling ciliary CP-MTs (Liu et al., 2021).

Importance of the Wdr47-Camsap interaction in the CP-MT formation

Next, we created an F260A point mutation in full-length Wdr47 and examined its association with Camsaps through co-immunoprecipitation. FLAG-tagged Camsap1 or Camsap3 displayed markedly reduced association with the GFP-tagged F260A mutant compared with the wild-type GFP-Wdr47 (Figures 4A and 4B). In contrast, the association of FLAG-Camsap2 with Wdr47 was only mildly compromised by the F260A mutation (Figures 4A and 4B). GFP-Wdr47 was previously shown to nicely rescue the CP-MT formation of cultured *Wdr47*$^{-/-}$ mouse ependymal cells (mEPCs) that are induced to undergo multiciliation through serum starvation (Liu et al., 2021).

To further verify the importance of the Wdr47-Camsap interaction, we expressed GFP-tagged wild-type Wdr47 (GFP-WT) and the F260A mutant (GFP-F260A) respectively, in *Wdr47*$^{-/-}$ mEPCs through lentiviral infection (Figure 4C; Liu et al., 2021) and fixed the cells at day 8. Due to the lack of an appropriate antibody to Camsap3, we examined the ciliary distributions of Camsap1 and Camsap2. Both GFP-WT and GFP-F260A localized into cilia (Figure S8A). Consistently (Liu et al., 2021), the expression of GFP-WT in *Wdr47*$^{-/-}$ mEPCs obviously increased the ciliary levels of Camsap1 and Camsap2 compared with uninfected *Wdr47*$^{-/-}$ mEPCs (Figures S8A and S8B). GFP-F260A, however, was less potent (Figures S8A and S8B). The average level of ciliary Camsap1 differed by 7-fold between the GFP-WT and GFP-F260A groups, whereas that of ciliary Camsap2 differed by 1.6-fold (Figure S8B). Therefore, the F260A mutation represses the ability of Wdr47 to recruit Camsap1 more severely than Camsap2, in accordance with the co-immunoprecipitation results (Figures 4A and 4B).

Consistent with the previous report (Liu et al., 2021), multicilia in uninfected *Wdr47*$^{-/-}$ mEPCs were completely absent of CP-MTs as indicated by the lack of ciliary immunofluorescent signals of Hydin (Figure 4D), a CP-MT marker (Lechtreck et al., 2008). In comparison, the majority of multicilia became Hydin positive in 70.7% of GFP-WT-positive *Wdr47*$^{-/-}$ mEPCs (Figure 4D), suggesting a high rescue efficiency on CP-MTs. 20.7% of the GFP-WT-positive cells displayed mild rescue effects, i.e., containing less but multiple (>3) Hydin-positive cilia. 66.7% of GFP-F260A-positive *Wdr47*$^{-/-}$ mEPCs, however, still completely lacked ciliary Hydin or just contained 1 or 2 Hydin-positive cilia (Figure 4D). 21.4% of them showed a mild rescue effect on the CP-MT formation (Figure 4D). Only 11.9% of them displayed a strong rescue effect. Therefore, the F260A mutation markedly reduced the rescue efficiency of Wdr47 on CP-MTs.

Multicilia of mEPCs typically beat in a back-and-forth (planar) manner. Due to the loss of CP-MTs, multicilia in *Wdr47*$^{-/-}$ mEPCs become rotatory (Liu et al., 2021). To corroborate the immunostaining results, we labeled ciliary axonemes of living mEPCs with SiR-tubulin, an MT-specific fluorescent dye (Lukinavicius et al., 2014), and examined the ciliary beat pattern through high-speed fluorescent imaging. Consistent with the previous report (Liu et al., 2021), multicilia of 68.8% of GFP-WT-positive *Wdr47*$^{-/-}$ mEPCs mainly displayed planar beat, and only 18.7% of the cells still contained multicilia that are mainly rotatory (Figures 4E and 4F; Video S1). In contrast, only 21.2% of them displayed multicilia of planar beat, and 58.5% of GFP-F260A-positive *Wdr47*$^{-/-}$ mEPCs still showed rotatory multicilia (Figures 4E and 4F; Video S2), consistent with their lack of CP-MTs. Taken together, these results confirmed the importance of the Wdr47-Camsap interaction in CP-MT formation.

The working model for Wdr47-mediated association of Camsaps in motile cilia

The non-centrosomal CP-MTs in the axoneme of motile cilia are essential for controlling ciliary motility (Loreng and Smith, 2017), but the underlying mechanism for the generation of

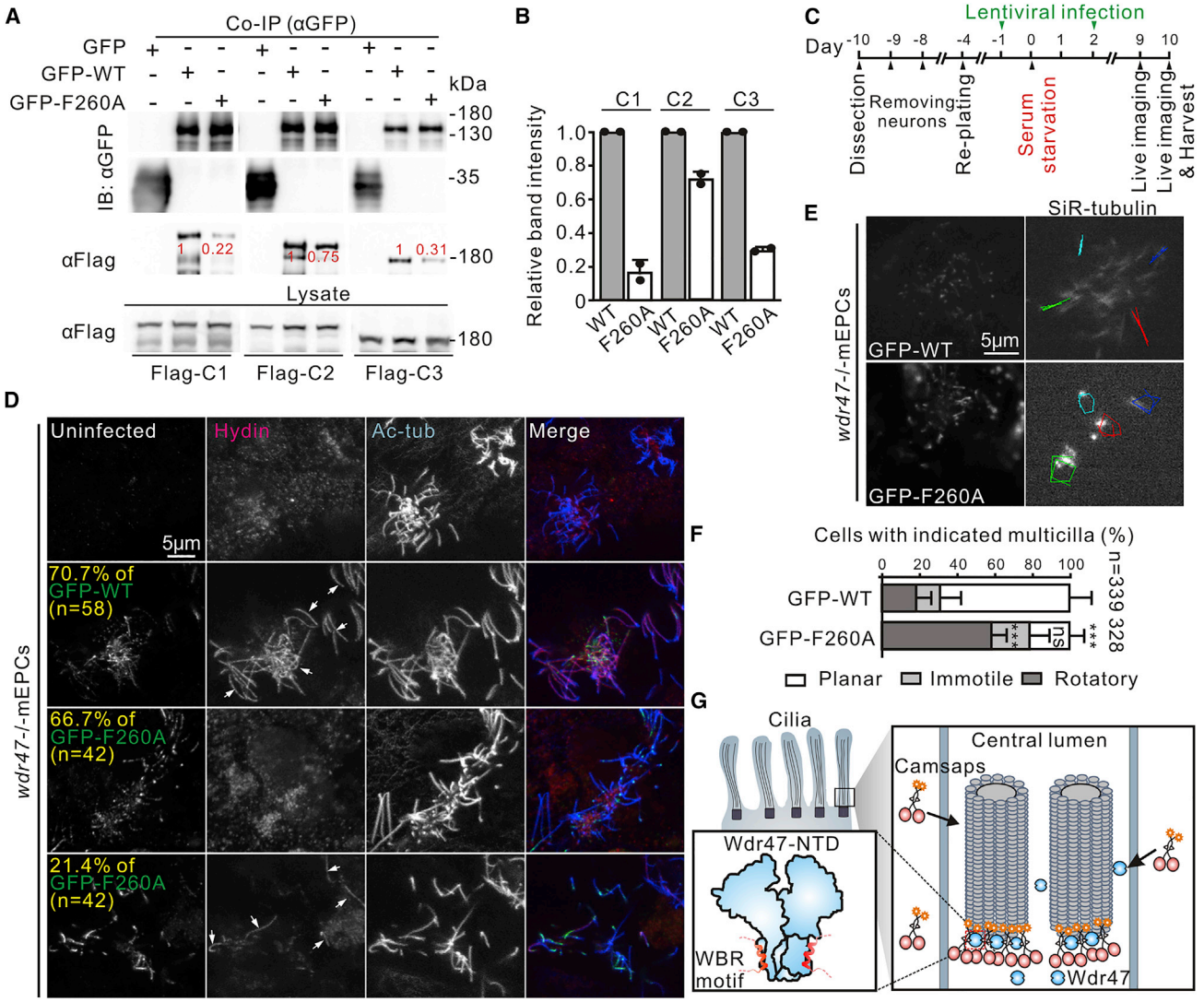

Figure 4. Wdr47-mediated recognition of Camsaps is essential for ciliary motility

(A and B) The F260A mutation attenuates the interaction of Wdr47 with full-length Camsaps. GFP or GFP-tagged wild-type Wdr47 (WT) or F260A mutant (F260A) was co-expressed with FLAG-tagged Camsap1 (C1), C2, or C3 in HEK293T cells. Co-immunoprecipitations (coIPs) were then performed using anti-GFP beads, followed by immunoblotting (A). Each set of images was cropped from the same blot. Relative band intensities of FLAG-Camsaps were quantified (A), and those from two independent experiments were presented in (B) as mean ± SD.

(C) Experimental scheme for the rescue experiments in (D) and (E). Radial gilia cultured from telencephala of E18.5 *Wdr47*$^{-/-}$ mice were serum starved at day 0 to induce differentiation into multiciliated mEPCs. Lentiviral infections were performed on days −1 and 2 to express GFP-WT or GFP-F260A. See STAR Methods for details.

(D) The F260A mutation impairs the rescue efficiency of Wdr47 on the CP formation. mEPCs cultured to day 10 (C) were harvested for immunostaining. Acetylated tubulin (Ac-tub) and Hydin serve as cilia and CP-MT markers, respectively. Arrows indicate typical Hydin-positive cilia or cilia clusters. Maximum intensity-projected images are presented.

(E and F) The F260A mutation reduces the ability of Wdr47 to restore the planar beat pattern of *Wdr47*$^{-/-}$ multicilia. Live imaging was performed at day 9 or 10 to trace motilities of SiR-tubulin-labeled multicilia in GFP-positive *Wdr47*$^{-/-}$ mEPCs. Maximum intensity-projected images are presented for GFP-WT or GFP-F260A, whereas the SiR-tubulin images were a single optical section. Trajectories of four representative cilia during the first 90 ms of live imaging are presented to show their beat patterns (E). Refer to Videos S1 and S2 for details. Quantification results (mean ± SD) (F) were from four independent experiments, each using mEPCs cultured from different embryos. At least 41 multiciliated cells were scored for each sample. One-way ANOVA and Turkey test: ns, no significance ($p > 0.05$); ***$p < 0.001$. Please note that as the autofluorescence of GFP was relatively weak, the z stack imaging only captured fluorescent signals at the immobile base regions of multicilia.

(G) A schematic working model for Wdr47-mediated association of Camsaps for controlling non-centrosomal CP-MTs in motile cilia. Briefly, Wdr47-NTD forms an intertwined dimer that specifically recognizes the basic helical WBR motif in Camsaps to recruit them into the central lumen of the axoneme. Since Camsaps most likely adopt a dimeric conformation through their CC segments, Wdr47-mediated association of Camsaps would further cross-link Camsaps to form a supramolecular complex to stabilize the minus ends of CP-MTs.

See also Figure S8.

CP-MTs remains largely unclear. Camsaps can stabilize MT minus ends for assembling non-centrosomal MTs, and Wdr47 is capable of recognizing Camsaps for generating CP-MTs (Akhmanova and Hoogenraad, 2015; Liu et al., 2021; Robinson et al., 2020). The binding between Wdr47 and Camsaps is mediated by Wdr47-NTD (featured with a LisH-CTLH motif) and a characteristic WBR motif in Camsaps (Figures 1 and 2). Unexpectedly, Wdr47-NTD forms an intertwined dimer through a special sub-domain organization and contains an expanded version of COR compared with other LisH-CTLH-containing domains (Figure 1). The expanded COR of Wdr47-NTD possesses a non-canonical target-binding site that specifically recognizes the basic helical WBR motif in Camsaps (Figures 2 and 3). This Wdr47-NTD-mediated recognition of the basic helical WBR motif is critical for the Wdr47-Camsap complex formation, CP-MT formation, and planar ciliary beat (Figure 4). Notably, although the F260A mutation in Wdr47-NTD abolished the interaction with Camsap3 (Figure 3E), the mutation did not completely disrupt the interactions of full-length Wdr47 with Camsaps (Figure 4A). This suggests that other regions outside Wdr47-NTD may also contribute to the interactions with Camsaps (possibly through the sites outside the WBR motif). Interestingly, although Camsap2 and Camsap3 are generally more homologous to each other than to Camsap1 (Hendershott and Vale, 2014), the critical residue R572 in the core WBR motif of Camsap3 is conserved only in Camsap1 (Figure 3F). As the Wdr47-Camsap2 interaction was only mildly attenuated by the F260A mutation (Figure 4A), this interaction may be specifically strengthened through the regions outside Wdr47-NTD and the WBR motif of Camsap2, consistent with recent studies of the binding between Wdr47 and Camsap2 (Buijs et al., 2021). Moreover, the similar binding affinities between Wdr47-NTD and the WBR peptides from three Camsaps may exclude the potential cause of different binding capacities by Wdr47-NTD (Figure S7C).

Based on this work and previous studies (Liu et al., 2021), a working model for Wdr47-mediated association of Camsaps for controlling non-centrosomal CP-MTs in motile cilia could be proposed (Figure 4G). In this working model, Wdr47 forms a stable dimer through the NTD, and Camsaps most likely also adopt a dimeric conformation due to the coiled-coil segments in the middle region (Figure 4G). The Wdr47-mediated association of Camsaps could recruit them into the central lumen of the axoneme for assembling non-centrosomal CP-MTs. Since Wdr47-NTD is an intertwined dimer, Wdr47-NTD-mediated recognition of the basic-helical WBR motif in Camsaps would further cross-link dimeric Camsaps to form a supra-molecular complex that could act as a scaffolding platform to grasp and stabilize the minus ends of CP-MTs (Figure 4G). Consistent with this proposal, Wdr47-NTD and the Camsap3 fragment, including the WBR motif and three coiled-coil segments (Camsap3-WBR-CC), could form a complex with a much larger molecular weight (Figure S8C), suggesting that the association of Wdr47-NTD with Camsap3-WBR-CC would lead to the formation of the supra-molecular complex.

In summary, this work reveals an unexpected intertwined Wdr47-NTD dimer and a non-canonical target-binding site in this LisH-CTLH-containing domain that can recognize a basic helical WBR motif in Camsaps for the Wdr47-Camsap complex assembly. The Wdr47-NTD dimer would cross-link dimeric Camsaps to assemble the high-order supra-molecular complex for controlling non-centrosomal CP-MTs. Interestingly, the WBR motifs of Camsap2 and Camsap3 are close to, but distinct from, their binding regions to katanin (Jiang et al., 2018), an MT-severing enzyme critical for the formation of both protozoan and mammalian CP-MTs (Dymek et al., 2004; Dymek and Smith, 2012; Liu et al., 2021). Whether Wdr47 and katanin could interfere with each other for binding to Camsaps is currently unclear.

Limitations of the study

Wdr47 can bind to three Camsaps and efficiently recruit them to the central lumen of the axoneme for proper CP-MT formation. The biochemical and structural characterizations of the binding between Wdr47-NTD and Camsap3 reveal the WBR motif in Camsaps for binding to the intertwined Wdr47-NTD dimer. However, since three Camsaps exhibit distinct binding capacities for full-length Wdr47, the biochemical and structural data derived from this study (with a focus on Wdr47-NTD) may only reflect a partial (but not full) picture of the Wdr47-Camsap complex formation. The overall assembly of the proposed supra-molecular complex with full-length proteins and the distinct binding features of different Camsaps warrant further structural and biochemical investigations.

STAR★METHODS

Detailed methods are provided in the online version of this paper and include the following:

- KEY RESOURCES TABLE
- RESOURCE AVAILABILITY
  - Lead contact
  - Material availability
  - Data and code availability
- EXPERIMENTAL MODEL AND SUBJECT DETAILS
  - Animals
  - Cell cultures
- METHOD DETAILS
  - Protein expression and purification
  - Size exclusion chromatography coupled with multi-angle light scattering (SEC-MALS)
  - Crystallization, data collection and structural determination
  - Isothermal titration calorimetry (ITC) assay
  - GST-pull down assay
  - Co-immunoprecipitation
  - mEPC infection
  - Fluorescent microscopy
- QUANTIFICATION AND STATISTICAL ANALYSIS

SUPPLEMENTAL INFORMATION

Supplemental information can be found online at https://doi.org/10.1016/j.celrep.2022.111589.

ACKNOWLEDGMENTS

We thank the Shanghai Synchrotron Radiation Facility for the beam time. This work was supported by grants from the National Key R&D Program of China (2017YFA0503500 to W.F., X.Z., and X.Y.), the Strategic Priority Research Program of CAS (XDB37020302 to W.F.), the National Natural Science Foundation of China (32071191 and 31829001 to W.F. and 31971160 to J.R.), the Chinese National Programs for Brain Science and Brain-like Intelligence Technology (2022ZD0205800 to J.R.), and the CAS Project for Young Scientists in Basic Research (grant no. 075 to J.R.).

AUTHOR CONTRIBUTIONS

J.R. and D.L. conducted experiments such as the protein purification, crystallization, diffraction data collection, structural determination, and other biochemical experiments with the supervision of W.F.; J.L. and H.L. performed cellular studies with the supervision of X.Y. and X.Z.; and W.F. and X.Z. interpreted the data and wrote the manuscript with input from all authors.

DECLARATION OF INTERESTS

The authors declare no competing interests.

Received: February 10, 2022
Revised: September 5, 2022
Accepted: October 11, 2022
Published: November 8, 2022

REFERENCES

Adams, P.D., Afonine, P.V., Bunkoczi, G., Chen, V.B., Davis, I.W., Echols, N., Headd, J.J., Hung, L.W., Kapral, G.J., Grosse-Kunstleve, R.W., et al. (2010). PHENIX: a comprehensive Python-based system for macromolecular structure solution. Acta crystallographica. Section D, Biological crystallography *66*, 213–221.

Akhmanova, A., and Hoogenraad, C.C. (2015). Microtubule minus-end-targeting proteins. Curr. Biol.: CB *25*, R162–R171.

Akhmanova, A., and Steinmetz, M.O. (2015). Control of microtubule organization and dynamics: two ends in the limelight. Nat. Rev. Mol. Cell Biol. *16*, 711–726.

Ashraf, U., Tengo, L., Le Corre, L., Fournier, G., Busca, P., McCarthy, A.A., Rameix-Welti, M.A., Gravier-Pelletier, C., Ruigrok, R.W.H., Jacob, Y., et al. (2019). Destabilization of the human RED-SMU1 splicing complex as a basis for host-directed antiinfluenza strategy. Procd. of the Natl Acad. of Sci. of the USA *116*, 10968–10977.

Atherton, J., Jiang, K., Stangier, M.M., Luo, Y., Hua, S., Houben, K., van Hooff, J.J.E., Joseph, A.P., Scarabelli, G., Grant, B.J., et al. (2017). A structural model for microtubule minus-end recognition and protection by CAMSAP proteins. Nat. Struct. Mol. Biol. *24*, 931–943.

Baines, A.J., Bignone, P.A., King, M.D., Maggs, A.M., Bennett, P.M., Pinder, J.C., and Phillips, G.W. (2009). The CKK domain (DUF1781) binds microtubules and defines the CAMSAP/ssp4 family of animal proteins. Mol. Biol. Evol. *26*, 2005–2014.

Brooks, E.R., and Wallingford, J.B. (2014). Multiciliated cells. Curr. Biol. : CB *24*, R973–R982.

Buijs, R.R., Hummel, J.J.A., Burute, M., Pan, X., Cao, Y., Stucchi, R., Altelaar, M., Akhmanova, A., Kapitein, L.C., and Hoogenraad, C.C. (2021). WDR47 protects neuronal microtubule minus ends from katanin-mediated severing. Cell Rep. *36*, 109371.

Chen, Y., Zheng, J., Li, X., Zhu, L., Shao, Z., Yan, X., and Zhu, X. (2020). Wdr47 controls neuronal polarization through the Camsap family microtubule minus-end-binding proteins. Cell Rep. *31*, 107526.

Delgehyr, N., Meunier, A., Faucourt, M., Bosch Grau, M., Strehl, L., Janke, C., and Spassky, N. (2015). Ependymal cell differentiation, from monociliated to multiciliated cells. Methods Cell Biol. *127*, 19–35.

Dymek, E.E., Lefebvre, P.A., and Smith, E.F. (2004). PF15p is the chlamydomonas homologue of the Katanin p80 subunit and is required for assembly of flagellar central microtubules. Eukaryot. Cell *3*, 870–879.

Dymek, E.E., and Smith, E.F. (2012). PF19 encodes the p60 catalytic subunit of katanin and is required for assembly of the flagellar central apparatus in Chlamydomonas. J. Cell Sci. *125*, 3357–3366.

Emes, R.D., and Ponting, C.P. (2001). A new sequence motif linking lissencephaly, Treacher Collins and oral-facial-digital type 1 syndromes, microtubule dynamics and cell migration. Hum. Mol. Genet. *10*, 2813–2820.

Emsley, P., and Cowtan, K. (2004). Coot: model-building tools for molecular graphics. Acta crystallographica. Section D, Biological crystallography *60*, 2126–2132.

Fliegauf, M., Benzing, T., and Omran, H. (2007). When cilia go bad: cilia defects and ciliopathies. Nat. Rev. Mol. Cell Biol. *8*, 880–893.

Ginger, M.L., Portman, N., and McKean, P.G. (2008). Swimming with protists: perception, motility and flagellum assembly. Nat. Rev. Microbiol. *6*, 838–850.

Hendershott, M.C., and Vale, R.D. (2014). Regulation of microtubule minus-end dynamics by CAMSAPs and Patronin. Prod. of the Natl. Acad. of Sci. of the USA *111*, 5860–5865.

Ishikawa, T. (2017). Axoneme structure from motile cilia. Cold Spring Harbor Perspect. Biol. *9*.

Jiang, K., Faltova, L., Hua, S., Capitani, G., Prota, A.E., Landgraf, C., Volkmer, R., Kammerer, R.A., Steinmetz, M.O., and Akhmanova, A. (2018). Structural basis of formation of the microtubule minus-end-Regulating CAMSAP-katanin complex. Structure *26*, 375–382.e374.

Jiang, K., Hua, S., Mohan, R., Grigoriev, I., Yau, K.W., Liu, Q., Katrukha, E.A., Altelaar, A.F., Heck, A.J., Hoogenraad, C.C., et al. (2014). Microtubule minus-end stabilization by polymerization-driven CAMSAP deposition. Dev. Cell *28*, 295–309.

Kannan, M., Bayam, E., Wagner, C., Rinaldi, B., Kretz, P.F., Tilly, P., Roos, M., McGillewie, L., Bar, S., Minocha, S., et al. (2017). WD40-repeat 47, a microtubule-associated protein, is essential for brain development and autophagy. Prod. of the Natl. Acad. of Sci. of the USA *114*, E9308–E9317.

Kimura, T., Saito, H., Kawasaki, M., and Takeichi, M. (2021). CAMSAP3 is required for mtorc1-dependent ependymal cell growth and lateral ventricle shaping in mouse brains. Development *148*. https://doi.org/10.1101/2020.07.19.211383.

Lechtreck, K.F., Delmotte, P., Robinson, M.L., Sanderson, M.J., and Witman, G.B. (2008). Mutations in Hydin impair ciliary motility in mice. The J. of cell Biol. *180*, 633–643.

Lechtreck, K.F., Gould, T.J., and Witman, G.B. (2013). Flagellar central pair assembly in Chlamydomonas reinhardtii. Cilia *2*, 15.

Lindemann, C.B. (2007). The geometric clutch as a working hypothesis for future research on cilia and flagella. Ann. N. Y. Acad. Sci. *1101*, 477–493.

Liu, H., Zheng, J., Zhu, L., Xie, L., Chen, Y., Zhang, Y., Zhang, W., Yin, Y., Peng, C., Zhou, J., et al. (2021). Wdr47, Camsaps, and Katanin cooperate to generate ciliary central microtubules. Nat. Commun. *12*, 5796.

Loreng, T.D., and Smith, E.F. (2017). The central apparatus of cilia and eukaryotic flagella. Cold Spring Harbor Perspect. Biol. *9*.

Lukinavicius, G., Reymond, L., D'Este, E., Masharina, A., Gottfert, F., Ta, H., Guther, A., Fournier, M., Rizzo, S., Waldmann, H., et al. (2014). Fluorogenic probes for live-cell imaging of the cytoskeleton. Nat. Methods *11*, 731–733.

Martin-Arevalillo, R., Nanao, M.H., Larrieu, A., Vinos-Poyo, T., Mast, D., Galvan-Ampudia, C., Brunoud, G., Vernoux, T., Dumas, R., and Parcy, F. (2017). Structure of the Arabidopsis TOPLESS corepressor provides insight into the evolution of transcriptional repression. Prod. of the Natl. Acad. of Sci. of the USA *114*, 8107–8112.

McCoy, A.J. (2007). Solving structures of protein complexes by molecular replacement with Phaser. Acta crystallographica. Section D, Biological crystallography *63*, 32–41.

Oda, T., Yanagisawa, H., Yagi, T., and Kikkawa, M. (2014). Mechanosignaling between central apparatus and radial spokes controls axonemal dynein activity. The J. of cell Biol. *204*, 807–819.

Otwinowski, Z., and Minor, W. (1997). Processing of X-ray diffraction data collected in oscillation mode. Methods Enzymol. *276*, 307–326.

Pongrakhananon, V., Saito, H., Hiver, S., Abe, T., Shioi, G., Meng, W., and Takeichi, M. (2018). CAMSAP3 maintains neuronal polarity through regulation of microtubule stability. Prod. of the Natl. Acad. of Sci. of the USA *115*, 9750–9755.

Praveen, K., Davis, E.E., and Katsanis, N. (2015). Unique among ciliopathies: primary ciliary dyskinesia, a motile cilia disorder. F1000prime reports *7*, 36.

Robinson, A.M., Takahashi, S., Brotslaw, E.J., Ahmad, A., Ferrer, E., Procissi, D., Richter, C.P., Cheatham, M.A., Mitchell, B.J., and Zheng, J. (2020). CAMSAP3 facilitates basal body polarity and the formation of the central pair of microtubules in motile cilia. Prod. of the Natl. Acad. of Sci. of the USA *117*, 13571–13579.

Satir, P., and Christensen, S.T. (2007). Overview of structure and function of mammalian cilia. Annu. Rev. Physiol. *69*, 377–400.

Satir, P., Heuser, T., and Sale, W.S. (2014). A structural basis for how motile cilia beat. Bioscience *64*, 1073–1083.

Schindelin, J., Arganda-Carreras, I., Frise, E., Kaynig, V., Longair, M., Pietzsch, T., Preibisch, S., Rueden, C., Saalfeld, S., Schmid, B., et al. (2012). Fiji: an open-source platform for biological-image analysis. Nat. Methods *9*, 676–682.

Stannard, W., Rutman, A., Wallis, C., and O'Callaghan, C. (2004). Central microtubular agenesis causing primary ciliary dyskinesia. Am. J. Respir. Crit. Care Med. *169*, 634–637.

Toya, M., Kobayashi, S., Kawasaki, M., Shioi, G., Kaneko, M., Ishiuchi, T., Misaki, K., Meng, W., and Takeichi, M. (2016). CAMSAP3 orients the apical-to-basal polarity of microtubule arrays in epithelial cells. Prod. of the Natl. Acad. of Sci. of the USA *113*, 332–337.

Ulrich, A.K.C., Schulz, J.F., Kamprad, A., Schutze, T., and Wahl, M.C. (2016). Structural basis for the functional coupling of the alternative splicing factors Smu1 and RED. Structure *24*, 762–773.

Usami, F.M., Arata, M., Shi, D., Oka, S., Higuchi, Y., Tissir, F., Takeichi, M., and Fujimori, T. (2021). Intercellular and intracellular cilia orientation is coordinated by CELSR1 and CAMSAP3 in oviduct multi-ciliated cells. J. Cell Sci. *134*.

Wang, Q.S., Zhang, K.H., Cui, Y., Wang, Z.J., Pan, Q.Y., Liu, K., Sun, B., Zhou, H., Li, M.J., Xu, Q., et al. (2018). Upgrade of macromolecular crystallography beamline BL17U1 at SSRF. Nucl. Sci. Tech. *29*.

Wang, W., Lundin, V.F., Millan, I., Zeng, A., Chen, X., Yang, J., Allen, E., Chen, N., Bach, G., Hsu, A., et al. (2012). Nemitin, a novel Map8/Map1s interacting protein with Wd40 repeats. PLoS One *7*, e33094.

Yau, K.W., van Beuningen, S.F., Cunha-Ferreira, I., Cloin, B.M., van Battum, E.Y., Will, L., Schatzle, P., Tas, R.P., van Krugten, J., Katrukha, E.A., et al. (2014). Microtubule minus-end binding protein CAMSAP2 controls axon specification and dendrite development. Neuron *82*, 1058–1073.

Zhang, Y., Chen, Y., Zheng, J., Wang, J., Duan, S., Zhang, W., Yan, X., and Zhu, X. (2019). Vertebrate Dynein-f depends on Wdr78 for axonemal localization and is essential for ciliary beat. J. Mol. Cell Biol. *11*, 383–394.

Zheng, J., Liu, H., Zhu, L., Chen, Y., Zhao, H., Zhang, W., Li, F., Xie, L., Yan, X., and Zhu, X. (2019). Microtubule-bundling protein Spef1 enables mammalian ciliary central apparatus formation. J. Mol. Cell Biol. *11*, 67–77.

Zhu, X., Liu, Y., and Yang, P. (2017). Radial spokes-A snapshot of the motility regulation, assembly, and evolution of cilia and flagella. Cold Spring Harbor Perspect. Biol. *9*.

STAR★METHODS

KEY RESOURCES TABLE

REAGENT or RESOURCE	SOURCE	IDENTIFIER
Antibodies		
Mouse anti-Acetylated Tubulin Monoclonal antibody	Sigma-Aldrich	Cat# T6793, RRID:AB_477585
Chicken anti-GFP Polyclonal Antibody	Invitrogen	Cat# A10262, RRID:AB_2534023
Guinea pig anti-Hydin	Zheng et al., 2019	N/A
Rabbit anti-Camsap1	Liu et al., 2021	N/A
Rabbit anti-Camsap2	Proeintech Group	Cat# 17880-1-AP, RRID:AB_2068826
Goat anti-Mouse IgG (H + L), Pacific Blue	Invitrogen	Cat# P31582, RRID:AB_10374586
Donkey anti-ChickenIgY (H + L),Alexa Fluor 488	Invitrogen	Cat# A-11039, RRID:AB_2534096
Donkey anti-guinea pigIgG (H + L), Cy3	Jackson ImmunoResearch	Cat# 706-165-148, RRID:AB_2340460
Goat anti-Rabbit IgG (H + L), Alexa Fluor 546	Invitrogen	Cat# A-11035, RRID:AB_2534093
Rabbit anti-GFP	Proeintech Group	Cat# 50430-2-AP, RRID:AB_11042881
Rabbit anti-Flag	Sigma-Aldrich	Cat# F7425, RRID:AB_439687
Goat anti-RabbitIgG (H + L), HRP	Invitrogen	Cat# G-21234, RRID:AB_2536530
Bacterial and virus strains		
DH5α Chemically Competent Cell	Ktsm-life	Cat# KTSM101
BL21(DE3) Chemically Competent Cell(*E.coli*)	TSINGKE	Cat# TSC-E01
Chemicals, peptides, and recombinant proteins		
Bovine Serum Albumins	Sigma	Cat# A7906
Glutathione Agrose Resin	Thermo Scientific	Cat# 16101
Tacsimate	Hampton research	Cat# HR2-827
Ethylene glycol	Hampton research	Cat# HR2-428-61
Lipofectamine 3000 reagent	Invitrogen	Cat# L3000-015
Dulbecco's Modified Eagle Medium (DMEM)	Gibco	Cat# 12430-054
Fetal bovine serum (FBS)	Ausbian	Cat# VS500T
Peptide: Camsap1 WBR	Beijing Scilight Biotechnology Led.Co.	N/A
Peptide: Camsap2 WBR	Beijing Scilight Biotechnology Led.Co.	N/A
Peptide: Camsap3 WBR	Beijing Scilight Biotechnology Led.Co.	N/A
Recombinant proteins: Wdr47-NTD (aa 1-315)	This paper	N/A
Recombinant proteins: Camsap3 (aa 1-350)	This paper	N/A
Recombinant proteins: Camsap3 (aa 351-593)	This paper	N/A
Recombinant proteins: Camsap3 (aa 594-950)	This paper	N/A
Recombinant proteins: Camsap3 (aa 951-1252)	This paper	N/A
Recombinant proteins: Camsap3 (aa 351-439)	This paper	N/A
Recombinant proteins: Camsap3 (aa 440-520)	This paper	N/A

(*Continued on next page*)

Continued

REAGENT or RESOURCE	SOURCE	IDENTIFIER
Recombinant proteins: Camsap3 (aa 521-593)	This paper	N/A
Recombinant proteins: Camsap3 (aa 561-590)	This paper	N/A
Recombinant proteins: GST-Wdr47 (aa 1-315)	This paper	N/A
Glutathione Sepharose 4B Fast Flow	GE Healthcare	Cat# 17513202
GFP-Trap Agarose	Chromotek	Cat# gta-20
Polyethyleneimine	Polysciences	Cat# 23966-2
Protease Inhibitor Cocktail Set III	Millipore	Cat# 539134
Papain	Worthington	Cat# LS003126
Glutamine	Sigma-Aldrich	Cat# G8540
Penicillin	Solarbio	Cat# P8010
Streptomycin	Solarbio	Cat# S8290
ProLong Diamond anti-fade mounting medium	Invitrogen	Cat# P36970
Superdex-200 26/60	GE healthcare	Cat# 17107101
BeyoZonase	Beyotime	Cat# D7121-5KU
Deposited data		
Crystal structure of Wdr47-NTD	Protein DataBank	PDB code: 7WEJ
Crystal structure of Wdr47-NTD/Camsap3 WBR-peptide	Protein DataBank	PDB code: 7WEK
Experimental models: Cell lines		
Human: HEK293T cells	ATCC	Cat# CRL-3216
Mouse: mEPC	This paper	N/A
Experimental models: Organisms/strains		
Mouse: Wdr47$^{-/-}$	Chen et al., 2020; Liu et al., 2021	N/A
Oligonucleotides		
Genotyping primer: Wildtype-forward	Chen et al., 2020; Liu et al., 2021	5′-TGTCTCCCTACCCTTCATCTC-3′
Genotyping primer: KO-backward	Chen et al., 2020; Liu et al., 2021	5′-CCAAATAGTCCTGCCATTAGTG-3′
Genotyping primer: KO-forward	Chen et al., 2020; Liu et al., 2021	5′-CAGCCATATCACATCTGTAGAG-3′
Genotyping primer: KO-backward	Chen et al., 2020; Liu et al., 2021	5′-CATGCCTTTAATCCCATCAC-3′
Recombinant DNA		
Plasmid: pET-32m3c-Wdr47 (aa 1-315)	This paper	N/A
Plasmid: pGEX-6p-1-Wdr47 (aa 1-315)	This paper	N/A
Plasmid: pET-32m3c-Camsap3 (aa 1-350)	This paper	N/A
Plasmid: pET-32m3c-Camsap3 (aa 351-593)	This paper	N/A
Plasmid: pET-32m3c-Camsap3 (aa 594-950)	This paper	N/A
Plasmid: pET-32m3c-Camsap3 (aa 951-1252)	This paper	N/A
Plasmid: pET-32m3c-Camsap3 (aa 351-439)	This paper	N/A
Plasmid: pET-32m3c-Camsap3 (aa 440-520)	This paper	N/A
Plasmid: pET-32m3c-Camsap3 (aa 521-593)	This paper	N/A
Plasmid: pET-32m3c-Camsap3 (aa 561-590)	This paper	N/A

(*Continued on next page*)

Continued

REAGENT or RESOURCE	SOURCE	IDENTIFIER
Plasmid: pET-32m3c-Camsap3 (aa 561-590)	This paper	N/A
Plasmid: pLV-GFP-Wdr47	This paper	N/A
Plasmid: pLV-GFP-Wdr47 F260A	This paper	N/A
Plasmid: pLV-Flag-C1-Camsap1	This paper	N/A
Plasmid: pLV-Flag-C1-Camsap2	This paper	N/A
Plasmid: pLV-Flag-C1-Camsap3	This paper	N/A
Software and algorithms		
HKL2000	Otwinowski and Minor, 1997	https://hkl-xray.com/hkl-2000
PHASER	McCoy, 2007	https://www.phaser.cimr.cam.ac.uk/index.php/Phaser_Crystallographic_Software
PHENIX	Adams et al., 2010	https://www.phenix-online.org/
COOT	Emsley and Cowtan, 2004	https://www2.mrc-lmb.cam.ac.uk/personal/pemsley/coot/
PYMOL	Molecular Graphics System,Schrodinger, LLC	https://pymol.org/2/
ASTRA	Wyatt Technology	https://www.wyatt.com/products/software/astra.htm
Origin 7.0	Microcal	https://microcal-origin.software.informer.com/
Fiji	Schindelin et al.,2012	https://imagej.net/software/fiji/

RESOURCE AVAILABILITY

Lead contact

Further information and requests for resources and reagents should be directed to and will be fulfilled by the Lead Contact, Wei Feng (wfeng@ibp.ac.cn).

Material availability

All the unique/stable reagents generated in this study are available from the lead contact with a completed materials transfer agreement.

Data and code availability

- All data reported in this paper will be shared by the lead contact upon request.
- This paper does not report original code.
- Any additional information required to reanalyze the data reported in this paper is available from the lead contact upon request.

EXPERIMENTAL MODEL AND SUBJECT DETAILS

Animals

Wdr47-deficient mice were constructed previously (Chen et al., 2020; Liu et al., 2021). Male and female $Wdr47^{+/-}$ mice of 3–10 months old were used for mating. As $Wdr47^{-/-}$ mice die of suffocation quickly after birth (Chen et al., 2020), E18.5 embryos were dissected for mEPC culture (see below). Genomic DNAs extracted from the mouse tails were used for genotyping with primers listed in KEY RESOURCES TABLE. When genotyping results were available, only cultured cells from $Wdr47^{-/-}$ embryos were maintained for further experiments.

Mice experiments were performed following the ethical guidelines of the Center for Excellence in Molecular Cell Science, Chinese Academy of Sciences, and approved by the institutional animal care and use committee.

Cell cultures

Multiciliated mEPCs were obtained and cultured as described (Delgehyr et al., 2015; Liu et al., 2021; Zhang et al., 2019; Zheng et al., 2019). Briefly, the telencephalon of each E18.5 mouse embryo was dissected in cold dissection solution (161 mM NaCl, 5 mM KCl, 1 mM $MgSO_4$, 3.7 mM $CaCl_2$, 5 mM HEPES, and 5.5 mM Glucose, pH 7.4) and digested with 1 mL of the dissection solution containing 10 U/ml papain (Worthington), 0.2 mg/ml L-Cysteine, 0.5 mM EDTA, 1 mM $CaCl_2$, 1.5 mM NaOH for 30 min at 37°C. Then

the dissection solution was replaced with culture medium, Dulbecco's Modified Eagle medium (DMEM, Gibco) supplemented with 10% fetal bovine serum (Ausbian), 0.3 mg/mL glutamine (Sigma), 100 U/ml penicillin (Solarbio), and 100 U/ml streptomycin (Solarbio). After gentle pipetting, the cells were plated on fibronectin (Millipore)-coated flask (Corning) and cultured in the culture medium at 37°C in 5% CO_2. Neurons were removed by flapping the flask at 24 h and 48 h. The remaining glial cells were cultured to approximately 80% confluency and transferred into fibronectin-coated 29-mm glass-bottom dishes (Cellvis), followed by serum starvation to induce multiciliation.

HEK293T cells were maintained at 37°C in an atmosphere containing 5% CO_2. The culture medium was Dulbecco's Modified Eagle medium (DMEM, Gibco) supplemented with 10% fetal bovine serum (Ausbian), 0.3 mg/mL glutamine (Sigma), 100 U/ml penicillin (Solarbio), and 100 U/ml streptomycin (Solarbio). HEK293T cells were used to express exogenous proteins for the biochemical analysis due to their high transfection efficiency.

METHOD DETAILS

Protein expression and purification

DNA sequences encoding Wdr47-NTD and various Camsap3 fragments were each cloned into a modified pET32a vector or a pGEX-6p-1 vector. The mutations in Wdr47-NTD were performed by using the standard PCR-based mutagenesis method and confirmed by DNA sequencing. Recombinant proteins were expressed in *Escherichia coli* BL21(DE3) host cells at 16°C. The GB1-His_6-tagged Wdr47-NTD and Trx-His_6-tagged Camsap3 fragments were purified by Ni^{2+}-Sepharose 6 Fast Flow (GE healthcare) affinity chromatography followed by size-exclusion chromatography (Superdex-200 26/60, GE healthcare). For Wdr47-NTD, after cleavage of the tag, the resulting proteins were further purified by another step of size-exclusion chromatography with the buffer containing 50 mM Tris-HCl, pH 8.0, 100 mM NaCl, 1 mM EDTA, 1 mM DTT. For Camsap3 fragments, recombinant proteins were purified in the same buffer without cleavage of the tag. The GST-tagged Wdr47-NTD used for the GST-pull down assay was purified by Pierce Glutathione Agarose Resin (Thermo Scientific) followed by size-exclusion chromatography (Superdex-200 26/60, GE healthcare).

The Wdr47-NTD/Camsap3-WBR-CC complex was obtained by co-purifying His_6-tagged Wdr47-NTD with Trx-His_6-tagged Camsap3-WBR-CC (residues from 561 to 937 of Camsap3) using the Ni^{2+}-Sepharose 6 Fast Flow (GE healthcare) affinity chromatography followed by size-exclusion chromatography (Superdex-200 26/60, GE healthcare).

Size exclusion chromatography coupled with multi-angle light scattering (SEC-MALS)

Protein samples (~1.0 mg/mL) were analyzed with static light scattering by injection of them into an Agilent HPLC system with a WTC SEC column (Wyatt Technology). The chromatography system was coupled with an 18-angle light-scattering detector (DAWN HELEOS II, Wyatt Technology) and differential refractive index detector (Optilab rEx, Wyatt Technology). Masses (molecular weights) were calculated with ASTRA (Wyatt Technology). BSA (Sigma) was used as the calibration standard.

Crystallization, data collection and structural determination

Purified Wdr47-NTD was concentrated to ~15 mg/mL in the buffer containing 50 mM Tris-HCl pH 8.0, 100 mM NaCl, 1 mM EDTA, and 1mM DTT for crystallization. Crystals of Wdr47-NTD were grown in 8% (v/v) Tacsimate pH 7.0, 20% (w/v) PEG-3350. For crystallization of the Wdr47-NTD/WBR-peptide complex, the commercially synthesized WBR-peptide was mixed with Wdr47-NTD (with the molar ratio of 2:1). Crystals of the Wdr47-NTD/WBR-peptide complex were grown in the 0.1 M Tris-HCl pH 8.5, 20% (w/v) PEG-3350. All the crystals were obtained using the vapor diffusion method (sitting drop) at 16°C. Before being flash-frozen in liquid nitrogen, crystals were cryo-protected in their mother liquor supplemented with 20% (v/v) ethylene glycol. Diffraction data were collected at the beamline BL19U at the Shanghai Synchrotron Radiation Facility (SSRF) with a wavelength of 0.979 Å at 100K (Wang et al., 2018), and were processed and scaled using HKL2000 (Otwinowski and Minor, 1997). The structure of Wdr47-NTD was determined by the SAD method with anomalous dispersion from the selenium atoms using AutoSol in PHENIX. Additional missing residues were manually modeled into the structure according to the 2Fo-Fc and Fo-Fc electron density maps. The structure of the Wdr47-NTD/WBR-peptide complex was determined by the molecular replacement method with the structure of Wdr47-NTD as the searching model using PHASER (McCoy, 2007). The WBR-peptide was manually modeled into the structure according to the 2Fo-Fc and Fo-Fc electron density maps. All the structures were further fitted and rebuilt with COOT (Emsley and Cowtan, 2004) and refined with PHENIX (Adams et al., 2010). The structure figures were prepared with the program PyMOL (https://pymol.org/2/). The statistics for data collection and structural refinement were summarized in Table 1. The atomic coordinates of apo-Wdr47-NTD and the Wdr47-NTD/WBR-peptide complex have been deposited in the Protein DataBank with the accession codes 7WEJ and 7WEK, respectively.

Isothermal titration calorimetry (ITC) assay

ITC assay was performed using a MicroCalorimeter ITC200 (GE Healthcare Life Sciences) at 25°C. Prior to the experiment, the protein samples were dialyzed in the buffer containing 50 mM Tris-HCl, pH 8.0, 100 mM NaCl, 1mM EDTA and 1mM DTT. Wdr47-NTD and its various mutants were put in the sample cell, while the synthesized WBR-peptide and its various mutants were in the syringe of the instrument. In each experiment, the peptide was sequentially injected into the stirred calorimeter cell initially containing the Wdr47-NTD protein sample with the injection sequence of 20 × 2 μL at 2 min intervals. The heat of dilution obtained by the titration

of the peptide into the buffer was subtracted. The integrated, corrected, and concentration-normalized peak areas of the raw data were finally fitted with a model of one binding site using ORIGIN 7.0 (OriginLab).

GST-pull down assay

To narrow down the minimal binding region within Camsap3 for Wdr47-NTD, GST, GST-tagged Wdr47-NTD and various Trx-tagged Camsap3 fragments were expressed in *Escherichia coli*. The cell suspensions were prepared in the PBS buffer containing various protease inhibitors. After centrifugation, the supernatant of GST or GST-tagged Wdr47-NTD were mixed with the supernatants of Trx-tagged Camsap3 fragments in the PBS buffer for 1 h at 4°C. The cleared mixtures were then incubated with 50 μL of Glutathione Sepharose 4B Fast Flow (GE Healthcare) 50% slurry beads for 3 h at 4°C. After washing the beads three times with the PBS buffer, the proteins captured by the beads were eluted by boiling with the SDS-PAGE sample buffer, resolved by SDS-PAGE and detected by Coomassie-blue staining.

For the binding to full-length Camsap3, the plasmids of Flag-tagged Camsap3 and its various mutants were transfected into HEK293T cells. Cells were collected 48 h after transfection. Cell pellets were lysed in the lysis buffer containing 50 mM Tris-HCl, pH 7.5, 150 mM NaCl, 1% NP-40, 1 mM EDTA, 1 mM PMSF, 10 mM DTT, 1× PhosStop (Roche), 250 U/ml BeyoZonase (Beyotime), 1× Protease Inhibitor Cocktail (Bimake). After centrifugation, the cleared supernatants were transferred to a batch of 50 μL 50% slurry beads, mixed with 130 μg GST or GST-tagged Wdr47-NTD for half an hour at 4°C. After washing the beads three times with the buffer containing 50 mM Tris-HCl, pH 7.5, 150 mM NaCl, 1% NP-40, 1 mM EDTA, 1 mM PMSF, 10 mM DTT, the proteins captured by the beads were eluted by boiling with the SDS-PAGE sample buffer. GST and GST-tagged Wdr47-NTD were detected by ponceau S staining and Flag-tagged Camsap3 proteins were analyzed by Western blot using the anti-Flag antibody (Proteintech).

Co-immunoprecipitation

pLV-GFP-Wdr47 was used to construct the F260A mutant through PCR. cDNAs of mouse Camsap1, Camsap2 and Camsap3 were amplified through PCR, cloned into pLV-Flag-C1 and verified by sequencing. HEK293T cells were used for the co-immunoprecipitation assay. The cells were co-transfected with plasmids using polyethyleneimine (PEI, Polysciences) to co-express GFP, GFP-Wdr47 or GFP-Wdr47(F260A) with Flag-tagged Camsap1, 2 or 3. The cells were lysed after 48 h with 600 μL of cold lysis buffer (20 mM Tris-HCl, pH 7.5, 100 mM KCl, 0.1% NP-40, 1 mM EDTA, 10 mM $Na_4P_2O_7$, 10% Glycerol, protease inhibitors cocktail (Millipore), 1 mM PMSF, 1 mM DTT, 5 mM NaF, and 1 mM Na_3VO_4). The cell lysates were cleared via centrifugation for 20 min at 13,000 rpm at 4°C, mixed with anti-GFP beads (Chromotek) and incubated overnight at 4°C under rotary agitation. The beads were washed three times with the lysis buffer and wash buffer (20 mM Tris-HCl, pH 7.5, 150 mM KCl, 0.5% NP-40, 1 mM EDTA, 10 mM $Na_4P_2O_7$, 10% Glycerol, protease inhibitors cocktail (Millipore), 1 mM PMSF, 1 mM DTT, 5 mM NaF, and 1 mM Na_3VO_4), respectively. Rabbit primary antibodies against GFP (Proteintech Group) and FLAG tag (Sigma-Aldrich) and Goat anti-Rabbit IgG-HRP (Life Technologies) were used for immunoblotting. Chemiluminescent signals were imaged using Mini-Chemiluminescent Imager (MiniChemi 610 Plus, Beijing Sage Creation Science Co).

mEPC infection

To express GFP-tagged Wdr47 and the F260A mutant in *Wdr47*$^{-/-}$ mEPCs for rescue experiments, lentiviral particles were packaged by transfecting lentiviral expression plasmids (10 μg), packaging plasmids pCMVdr8.9 (8 μg) and pMD2.VSVG (6 μg) into HEK293T cells. After 48 h, lentiviral particles were pelleted from culture media through ultracentrifugation at 92,800 ×*g* (Hitachi High-Technologies) for 2 h at 4°C, suspended in DMEM and stored at −80°C in aliquots. *Wdr47*$^{-/-}$ mEPCs were infected with lentivirus at one day before serum starvation (day −1) and 2 days after serum starvation (day 2).

Fluorescent microscopy

For immunofluorescent staining, mEPCs cultured to day 10 were washed with PBS and pre-extracted with 0.5% Triton X-100 in PBS for 30 s at room temperature, followed by fixation with 4% paraformaldehyde in PBS for 15 min at room temperature and permeabilization with 0.5% Triton X-100 for 15 min. After blocking with 4% BSA in PBS for 1 h, the samples were incubated with primary antibodies at 4°C overnight, washed with 4% BSA in PBS and incubated with second antibodies for 1 h at room temperature. After serial washes with 4% BSA in PBS and PBS, the samples were mounted with ProLong Diamond anti-fade mounting medium (Invitrogen). Confocal images were captured using a Leica TCS SP8 system with a 63×/1.40 oil immersion objective. Primary antibodies were chicken anti-GFP IgY (1:200; Invitrogen), mouse anti-acetylated tubulin mAb (1:1000; Sigma-Aldrich), rabbit anti-Camsap1 (1:100; home-made) (Liu et al., 2021), rabbit anti-Camsap2 (1:100; Proeintech Group) and guinea pig anti-Hydin antibody (1:200; home-made) (Zheng et al., 2019). Secondary antibodies were donkey anti-chicken IgY-Alexa Fluor 488 (1:1000; Invitrogen), donkey anti-guinea pig IgG (H + L)-Cy3 (1:1000; Jackson ImmunoResearch), goat anti-rabbit IgG (H + L)-Alexa Fluor 546 (1:1000; Invitrogen) and goat anti-mouse IgG (H + L)-Pacific blue (1:500; Invitrogen). Ciliary intensity of immunofluorescence was quantified from single cilium as described previously (Liu et al., 2021). Relative level of ciliary Camsap1 or Camsap2 was obtained by normalizing the immunofluorescent intensity to that of acetylated tubulin (Ac-tub) in the same region of a cilium.

For live imaging, multicilia of mEPCs cultured to day 9 or day 10 were labeled with SiR-tubulin (100 nM final concentration; Spirochrome) in the culture medium for 1 h at 37°C. After a snapshot of z-slices to locate GFP-positive cells, ciliary motilities at an appropriate z-plane were recorded at 10 ms-intervals for 200 frames by using an Olympus SpinSR microscope with a

60×/1.42 NA oil immersion objective. Ciliary beat patterns were analyzed using Fiji (NIH) (Schindelin et al., 2012). Multicilia were considered to beat in a planar or rotatory pattern or be immotile through their predominant behaviors.

QUANTIFICATION AND STATISTICAL ANALYSIS

All the details about the statistical tests that were performed in this study can be found in the figure legends. All the data processing and statistical analysis were performed using Excel (Microsoft) and GraphPad Prism (GraphPad Software). Significance was defined as follows: ns, no significance ($p > 0.05$); ***$p < 0.001$; ****$p < 0.0001$. All the graphs were generated using GraphPad Prism (GraphPad Software).